Electrochimica Acta 209 (2016) 278–284

Contents lists available at ScienceDirect

Electrochimica Acta

journal homepage: www.elsevier.com/locate/electacta

Enhancement of the electrochemical performance of silicon anodes through alloying with inert metals and encapsulation by graphene nanosheets

Sang-Hyung Kim[a], Seung-Hyun Yook[a], Aravindaraj G. Kannan[a], Seon Kyung Kim[b], Cheolho Park[b], Dong-Won Kim[a,*]

[a] Department of Chemical Engineering, Hanyang University, Seoul 133-791, South Korea
[b] Next-G Institute of Technology, Iljin Electric Co., Ltd., Gyeonggi-do 425-100, South Korea

ARTICLE INFO

Article history:
Received 24 February 2016
Received in revised form 20 April 2016
Accepted 11 May 2016
Available online 12 May 2016

Keywords:
Silicon alloy
Reduced graphene oxide
Electrochemical performance
Lithium-ion battery
Encapsulation

ABSTRACT

Silicon alloys composed of silicon nanoparticles embedded in inert Cu-Al-Fe matrix phases were synthesized and encapsulated with reduced graphene oxide (rGO) nanosheets. Successful synthesis of the silicon alloys and their encapsulation with rGO were confirmed by X-ray diffraction, X-ray photoelectron spectroscopy and transmission electron microscopic analyses. The silicon alloy encapsulated with an optimal amount of rGO delivered an initial discharge capacity of 1140.7 mAh g^{-1} with good capacity retention and exhibited excellent rate capability. This superior performance could be attributed to the unique structure of silicon alloy encapsulated by rGO, which could effectively accommodate the large volume change during cycling and provide continuous electronic conduction pathway in the electrode.

1. Introduction

High energy density lithium-ion batteries for electric vehicles and large-scale energy storage systems require significant improvement in the specific capacity of the electrode materials [1–5]. In this regard, silicon is considered to be a promising anode material in lithium-ion batteries, because it has a high theoretical capacity, low reduction potential, is cost-effective due to its natural abundance, and is non-toxic. However, the practical application of silicon materials in lithium-ion batteries is hampered by the large volume changes that occur during repeated lithiation/delithiation, which result in the cracking of the electrode, loss of electrical contact, unstable solid electrolyte interphase (SEI) formation, and eventually rapid capacity fading upon cycling [6,7]. The effect of volume changes on the cycling performance of silicon anodes has been largely addressed by nano-structured silicon materials with various shapes and morphologies, including nanowires, thin films, hollow structures and nanotubes [8–12]. However, their large surface area causes uncontrollable side reactions and reduces volumetric energy density, both of which critically limit their practical application [13]. The cycling performance of silicon materials has also been improved by using polymeric binders with enhanced binding characteristics and self-healing properties [14–17]. Another promising approach is the utilization of active-inactive alloy systems, where the electrochemical reaction occurs in the active phase and the inactive phase helps to improve electronic conductivity and acts as a volume buffer [18,19]. Composites of silicon nanoparticles and graphene have also been shown to be good candidates as anode material [20–28]. In particular, the utilization of graphene to improve the electrochemical performance of silicon-based electrodes is becoming increasingly appealing due to its superior properties such as good mechanical strength, high electronic conductivity, high chemical stability and good flexibility [29–31]. However, to the best of our knowledge, silicon alloys composed of active and inactive metals have not been encapsulated with graphene to exploit the beneficial effects of these systems.

In this work, we synthesized silicon alloys composed of silicon nanoparticles embedded in Cu-Al-Fe matrix phases. The resulting micron-sized silicon alloy particles were encapsulated with reduced graphene oxide (rGO) to mitigate the deleterious effects caused by volume changes during lithiation/delithiation as well as to provide a continuous electronic conduction pathway in the electrode. This strategy resulted in enhanced cycling performance in terms of discharge capacity, capacity retention and rate capability.

* Corresponding author. Tel.: +82 2 2220 2337; fax: +82 2 2298 4101.
E-mail address: dongwonkim@hanyang.ac.kr (D.-W. Kim).

http://dx.doi.org/10.1016/j.electacta.2016.05.081
0013-4686/

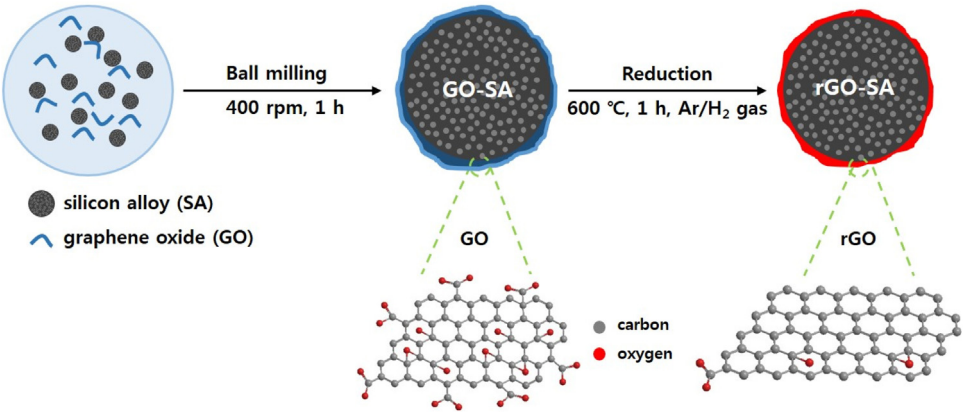

Fig. 1. Schematic illustration for encapsulation of the silicon alloy with rGO.

2. Experimental

2.1. Materials synthesis

Silicon alloy materials were synthesized using arc melting followed by the single roll solidification method (SRSM), as reported previously [19]. Si (50 at.%), Cu (22.5 at.%), Al (22.5 at.%), and Fe (5 at.%) metals were used as precursors to synthesize the silicon alloys. Copper, aluminum and iron metals were chosen as the inactive components of the alloy matrix due to their low cost and wide availability. Alloy buttons were obtained by arc melting in a Cu hearth using a non-consumable tungsten electrode under an argon atmosphere. The buttons were re-melted three times to ensure homogeneity. SRSM ribbons were produced by a graphite nozzle single-roll method under an inert atmosphere to prevent oxidation. The obtained ribbons were mechanically crushed into silicon alloy powders in an attrition mill at a rotating speed of 150 rpm with zirconia beads. Graphite oxide was prepared using the two-step modified Hummer's method from graphite powder (SP-1, 30 μm nominal particle size, Bay Carbon, USA). Pre-oxidation of graphite was carried out as reported by Kovtyukhova et al. [32], followed by oxidation using the Hummer's method [33]. Graphene oxide (GO) was finally obtained by exfoliating the prepared graphite oxide using ultrasonication. The as-prepared silicon alloy particles were encapsulated with rGO sheets in two steps, as illustrated in Fig. 1. In the first step, a proper amount of silicon alloy and GO was dispersed in ethanol, and the resulting solution was mixed using planetary ball-milling at 400 rpm for 1 h. The contents of GO in the mixed solutions were 5, 10, and 15 wt.% based on the weight of the silicon alloy materials. The mixtures were then dried to form GO-coated silicon alloys (hereafter referred to as GO(x)-SA, where x denotes the wt.% of GO), followed by thermal reduction at 600 °C for 1 h in an Ar/H_2 (96/4) atmosphere to reduce GO. Finally, rGO-encapsulated silicon alloys (hereafter referred to as rGO(x)-SA) were obtained.

2.2. Electrode preparation and cell assembly

The silicon alloy electrodes were prepared by coating a viscous slurry containing 86.6 wt.% silicon alloy (pristine silicon alloy or rGO(x)-SA), 3.4 wt.% Ketjen black and 10 wt.% poly(amide imide) (PAI, HV 4000 T, Solvay) dissolved in N-methyl-2-pyrrolidone

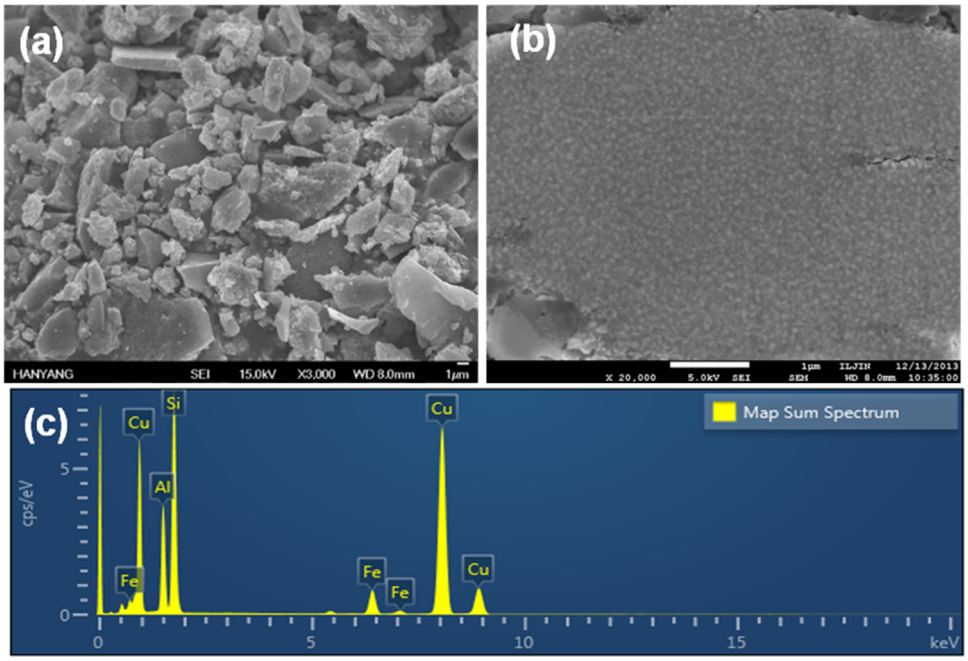

Fig. 2. (a) SEM and (b) cross-sectional SEM images of silicon alloy particles, and (c) the corresponding SEM-EDS spectrum.

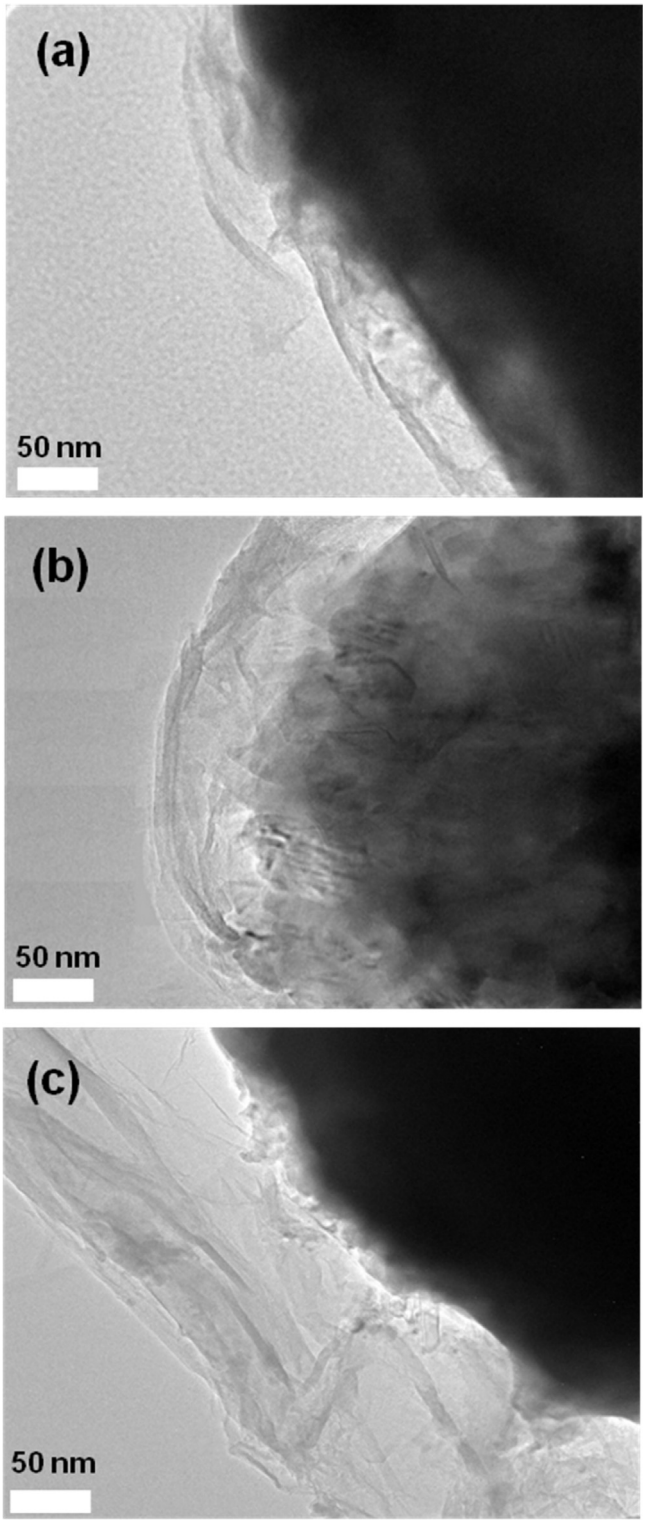

Fig. 3. TEM images of (a) rGO(5)-SA, (b) rGO(10)-SA and (c) rGO(15)-SA particles.

(NMP) onto copper foil. The cast slurry was dried in a vacuum oven at 90 °C for 1 h to evaporate the NMP solvent. The dried electrodes were then thermally treated to enhance particulate contact and adhesion to the current collector at 300 °C in a tube furnace for 1 h under an Ar atmosphere. As a control sample, the electrode with GO-coated silicon alloy (GO(x)-SA) was also prepared using the same procedure. Active mass loading in the silicon alloy electrodes corresponded to a capacity of 1.6 mAh cm^{-2}. To evaluate the cycling characteristics of silicon alloy electrodes, a CR2032-type coin cell was assembled by sandwiching a polyethylene (PE) separator (ND420, thickness: 20 μm, Asahi Kasei E-materials) between the metallic lithium counter electrode and the silicon alloy working electrode. The lithium electrode consisted of 100 μm-thick lithium foil (Honjo Metal Co. Ltd.) pressed onto a copper current collector. The cell was then injected with an electrolyte solution consisting of 1.15 M $LiPF_6$ in ethylene carbonate (EC)/ethylmethyl carbonate (EMC)/diethyl carbonate (DEC) (3/5/2 by volume) containing 5 wt. % fluoroethylene carbonate (FEC) (battery grade, PANAX ETEC Co. Ltd.). All cells were assembled in a dry box filled with argon gas.

2.3. Characterization and measurements

The morphology of the prepared samples was characterized using scanning electron microscopy (SEM, JEOL JSM 6701F), transmission electron microscopy (TEM, JEOL, JEM 2100F), and energy dispersive X-ray spectroscopy (EDS). To examine the cross-sectional morphologies of the silicon alloy materials and the silicon alloy electrodes, the samples were cut using an argon-ion beam polisher (JEOL, IB-09010CP) at a constant power under an inert Ar atmosphere to avoid chemical damage. X-ray photoelectron spectroscopy (XPS, VG multilab ESCA system, 220i) was used to examine the nature and quantify the degree of GO reduction. X-ray diffraction (XRD) patterns were obtained using a Rigaku D/MAX 2500 diffractometer in the scan range of 5 to 80°. Charge and discharge cycling tests of the silicon alloy electrodes were carried out at a current density of 0.32 mA cm^{-2} (0.2C rate) over a voltage range of 0.005 to 1.5 V using battery test equipment (WBCS 3000, WonA Tech Co., Ltd.), unless otherwise specified. We hereafter refer to lithiation as the charge and delithiation as the discharge, based on the practical applications of lithium-ion batteries. During the charging cycles, lithiation was performed at a 0.2C rate to a set voltage of 0.005 V. This was followed by charging at constant voltage until the final current reached 10% of the charging current. All electrochemical measurements were carried out at 25 °C and the specific capacity was based on the mass of silicon alloy material in the electrode.

3. Results and discussion

Fig. 2(a) shows the morphology of the synthesized silicon alloy particles confirming that micron-sized particles were observed. Cross-section polished-SEM analysis was performed using an argon-ion beam polisher to observe the microstructure of the silicon alloy material. As shown in Fig. 2(b), the silicon alloy was composed of two different phases. According to EDS analysis, the

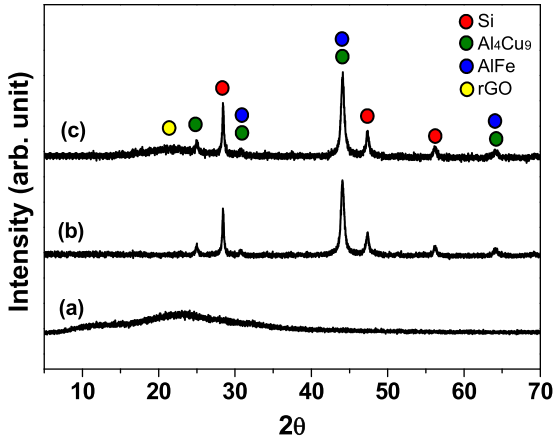

Fig. 4. XRD patterns of (a) rGO, (b) pristine silicon alloy and (c) rGO(10)-SA samples.

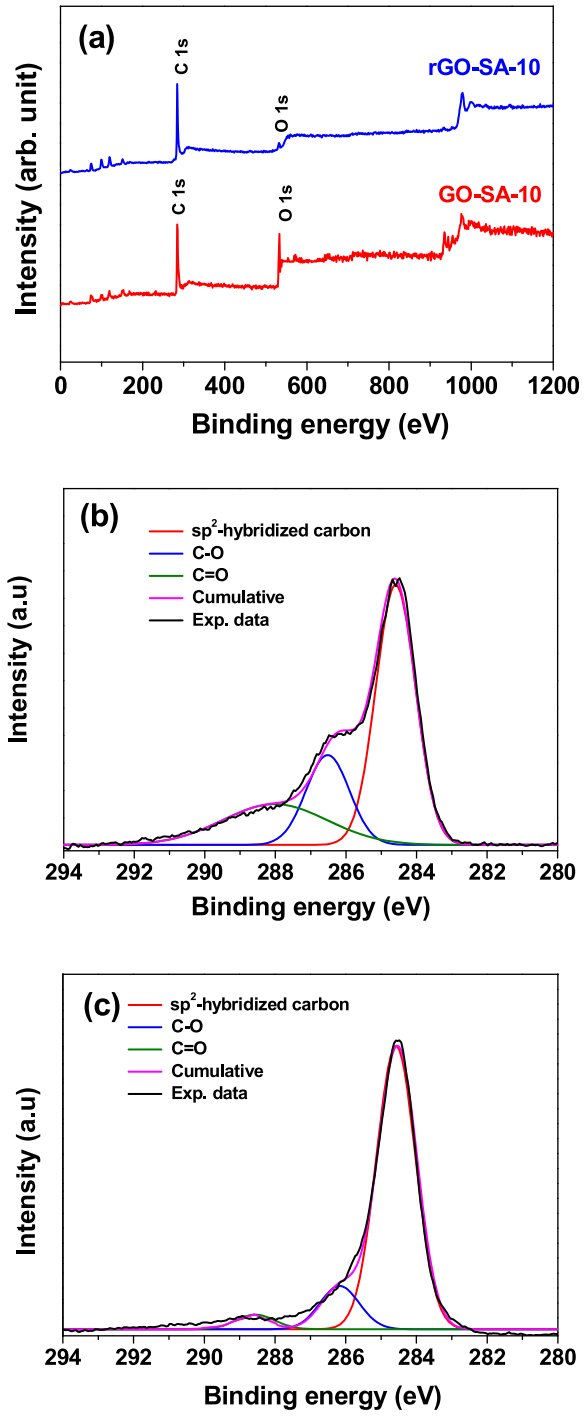

Fig. 5. (a) XPS survey spectra of GO(10)-SA and rGO(10)-SA samples. High-resolution XPS C 1s spectra of (b) GO(10)-SA and (c) rGO(10)-SA samples.

dark regions were silicon crystallites, while the light parts corresponded to inert metal phases composed of Al_4Cu_9 and AlFe [19]. The distribution of silicon in the alloy was found to be very uniform. The SEM-EDS spectrum presented in Fig. 2(c) revealed that the silicon alloy consisted of 50.6 at.% Si, 22.4 at.% Al, 22.3 at.% Cu, and 4.7 at.% Fe. This result matched well with the atomic percentages of the elements in the initial precursor mixture.

TEM images of the silicon alloys encapsulated by different amounts of rGO are shown in Fig. 3. Images of the edge of the silicon alloy particles revealed that they were fully encapsulated by the rGO layer. We propose the following encapsulation mechanism based on previous work by Yan et al. [34]. During the ball-milling process, the silicon alloy particles were broken and their surface activated. Surface activation facilitated strong interaction between the silicon alloy particles and GO, leading to GO bending around the silicon alloy particles. As shown in Fig. 3, the rGO coating layer increased in thickness as the amount of rGO increased. As compared to conventional metal-oxide coating which yields discontinuous deposition of an electrically inert layer, the rGO layer showed highly continuous surface coverage with some void space. The void space could act as an efficient buffer of volume changes during cycling. To examine whether electrical conductivity was enhanced by rGO encapsulation, the electronic conductivity of two kinds of electrodes without conducting carbon was measured using the four-point method. The electronic conductivities of the film prepared with 90 wt.% rGO(10)-SA and 10 wt.% PAI binder was 147.2 S cm^{-1}, which was higher than that of the film prepared with same content of pristine silicon alloy particles and PAI binder (24.5 S cm^{-1}). These results indicated that full encapsulation of the silicon alloy particles by rGO provided continuous electronic conduction pathways in the electrode.

The crystalline structures of rGO, pristine silicon alloy and rGO (10)-SA samples were characterized using XRD measurements, and the results are shown in Fig. 4. The broad diffraction peak observed in the range of 19 to 26° in rGO indicates poor ordering of the graphene sheets. The pristine silicon alloy showed many crystalline peaks, which were assigned to crystalline Si, AlFe alloy, and Al_4Cu_9 alloy phases [19]. The major diffraction peaks observed at 28.5, 47.5, and 56.3° were indexed to the lattice planes of (111), (220), and (311) of silicon (JCPDS no. 27-1402) [22]. The peak positions in the XRD pattern of the rGO(10)-SA sample were identical to those of a simple combination of the crystalline peaks corresponding to rGO and pristine silicon alloy. This result suggests that the silicon alloy particles were efficiently embedded in the rGO sheets and that reduction of GO-SA to rGO-SA did not destroy the crystalline structures of the silicon alloy. To further investigate the extent of reduction GO-SA to rGO-SA, XPS analysis was carried out, and the resulting spectra are shown in Fig. 5. XPS survey spectra of GO(10)-SA and rGO(10)-SA in Fig. 5(a) show the presence of C 1s and O 1s peaks. The C/O ratios in GO(10)-SA and rGO(10)-SA were calculated to be 1.66 and 16.24, respectively. The higher C/O ratio in rGO(10)-SA than GO(10)-SA indicates that the oxide groups present on the GO surface were highly reduced during the thermal reduction process. As shown in Figs. 5(b) and (c), the high resolution C1s spectra of GO(10)-SA and rGO(10)-SA could be resolved into three peaks centered at 284.5, 286.6, and 288.6 eV, which could be assigned to sp^2-hybridized carbon, C—O (hydroxyl/epoxy), and C=O (carbonyl/carboxyl), respectively [35,36]. The intensities of the C—O and C=O peaks were markedly decreased in the rGO(10)-SA sample in comparison to the GO(10)-SA sample, indicating effective removal of oxygen functional groups such as epoxy, hydroxyl, carbonyl, and carboxyl groups as a result of the reduction of GO into rGO.

The silicon alloy electrodes were initially subjected to a preconditioning cycle at a 0.1C rate prior to cycling tests. Fig. 6(a) shows the first charge and discharge curves of the pristine silicon alloy and rGO(x)-SA electrodes, which are obtained in the preconditioning cycle. All electrodes exhibited typical charge and discharge profiles corresponding to lithiation of Si and delithiation of Li_xSi, respectively. The initial charge and discharge capacities of the pristine silicon alloy electrode were 1384.6 and 1152.3 mAh g^{-1} based on the mass of silicon alloy material in the electrode, respectively, with a coulombic efficiency of 83.2%. The initial discharge capacity corresponds to a volumetric capacity of 4263.5 mAh cm^{-3} based on the volume of silicon alloy material, which is much higher than that (719 mAh cm^{-3}) of commercialized graphite active materials [37]. The irreversible capacity observed

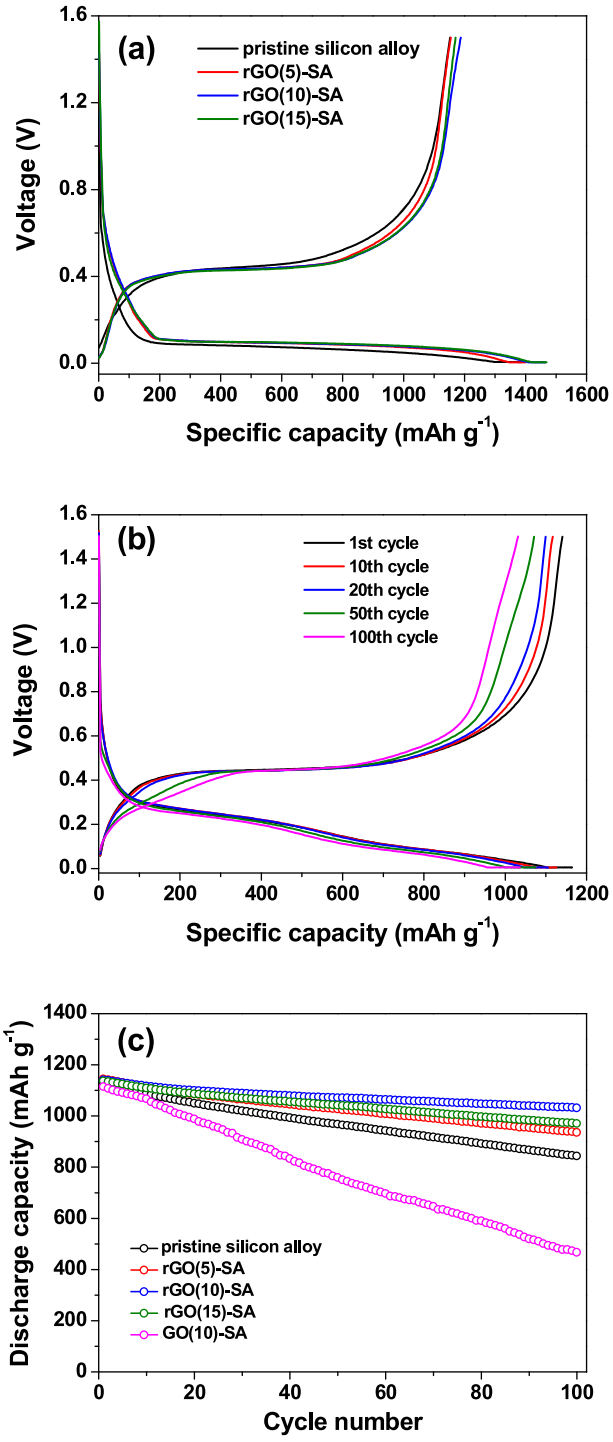

Fig. 6. (a) Initial charge and discharge curves of different silicon alloy electrodes. (Conditions: 0.1C constant current (CC) and constant voltage (CV) charge, 0.1C CC discharge, cut-off voltage: 0.005–1.5 V). (b) Charge and discharge curves of the rGO (10)-SA electrode, and (c) discharge capacities of different silicon alloy electrodes as a function of cycle number. (Conditions: 0.2C CC and CV charge, 0.2C CC discharge, cut-off voltage: 0.005–1.5 V).

in the first cycle was attributed to SEI layer formation due to reductive decomposition of the liquid electrolyte [38,39]. Coulombic efficiencies decreased with an increase in the amount of rGO. This result could be ascribed to the formation of a SEI layer on the rGO nanosheets with a large surface area, and the reaction of oxygen-containing functional groups on rGO with lithium ions [40]. The other difference in the charge and discharge voltage profiles was the reduction of overpotential in the rGO(x)-SA electrodes in comparison to the pristine silicon alloy electrodes, indicating facile charge transport in the rGO(x)-SA electrodes. We attributed this to the rGO coated on the silicon alloy particles acting as a bridge to connect neighboring particles and providing a continuous electronic conduction pathway, resulting in a decrease in overpotential during cycling. After two preconditioning cycles at a 0.1C rate, cells were cycled in the voltage range of 0.005 to 1.5 V at a 0.2C rate. Fig. 6(b) shows the charge and discharge curves of the electrode with rGO(10)-SA at 25 °C. The rGO(10)-SA electrode initially delivered a discharge capacity of 1140.7 mAh g^{-1} with a coulombic efficiency of 98.0%. After 100 cycles, the discharge capacity decreased to 1031.7 mAh g^{-1}, which corresponds to 90.4% of the initial discharge capacity. Such a good stability can be ascribed to the unique rGO(x)-SA structure, where both the inert metals in the silicon alloy and the flexible graphene layer acted as buffers for volume changes, resulting in enhancement of the structural stability of the electrode. In addition, complete encapsulation of the silicon alloy by rGO prevented direct contact between the silicon alloy and the electrolyte, thus suppressing continuous growth of the SEI layer that may degrade the electrochemical performance. Coulombic efficiency increased steadily with cycling, and it was maintained at over 99.0% during cycling, indicating good stability of the SEI layer and electrode structure. Fig. 6(c) shows the discharge capacities of the pristine silicon alloy and rGO(x)-SA electrodes during 100 cycles at a 0.2C rate. The pristine silicon alloy electrode showed relative stable performance due to the presence of an inactive matrix to suppress the volume expansion of silicon. However, its capacity fading was faster than that of the rGO(x)-SA electrodes, and the discharge capacity dropped to 74.6% after 100 cycles. Encapsulation of the silicon alloy by rGO coating improved cycling stability, and the rGO (10)-SA electrode showed the best capacity retention among the electrodes investigated. We attributed the improvement in capacity retention of the rGO(x)-SA electrodes to the synergistic effects of inert metals in the alloy structure and encapsulation with a flexible rGO sheet. The void space in the rGO layer surrounding the silicon alloy could accommodate volume expansion/contraction during lithiation/delithiation, making the silicon alloy electrode more tolerant to mechanical stress and maintaining its integrity during repeated cycling. As mentioned earlier, the rGO layer also allowed good electrical contact between the silicon alloy active materials to be maintained, which led to good capacity retention. However, the rGO(15)-SA electrode had a thick rGO layer encapsulating the silicon alloy particles, which hindered Li^+-ion transport through the rGO layer and thereby exerted a negative influence on cell performance. Based on these results, we concluded that the optimum content of rGO to obtain the best cycling stability was 10 wt.% based on weight of the silicon alloy. In order to clarify advantages of encapsulation of silicon alloy using rGO, we evaluated the cycling performance of the GO(10)-SA electrode, and the results are also shown in Fig. 6(c). As shown, the GO(10)-SA electrode showed inferior cycling performance in comparison to the pristine silicon alloy and rGO(x)-SA electrodes. This result demonstrates the negative influence of GO coating on the electrochemical performance of silicon alloy electrode, because the GO layer on silicon alloy may hamper the electron transfer into the silicon alloy due to its insulating nature.

Cross-sectional SEM images of pristine silicon alloy and rGO (10)-SA electrodes after 100 cycles were examined. The pristine silicon alloy electrode exhibited large voids and cracks between the electrode and current collector (Fig. 7(a)), which arose from large volume changes during the charge and discharge cycles. The loss of electrical conduction paths in this electrode was likely the main cause of the large degradation in capacity shown in Fig. 6(c). In

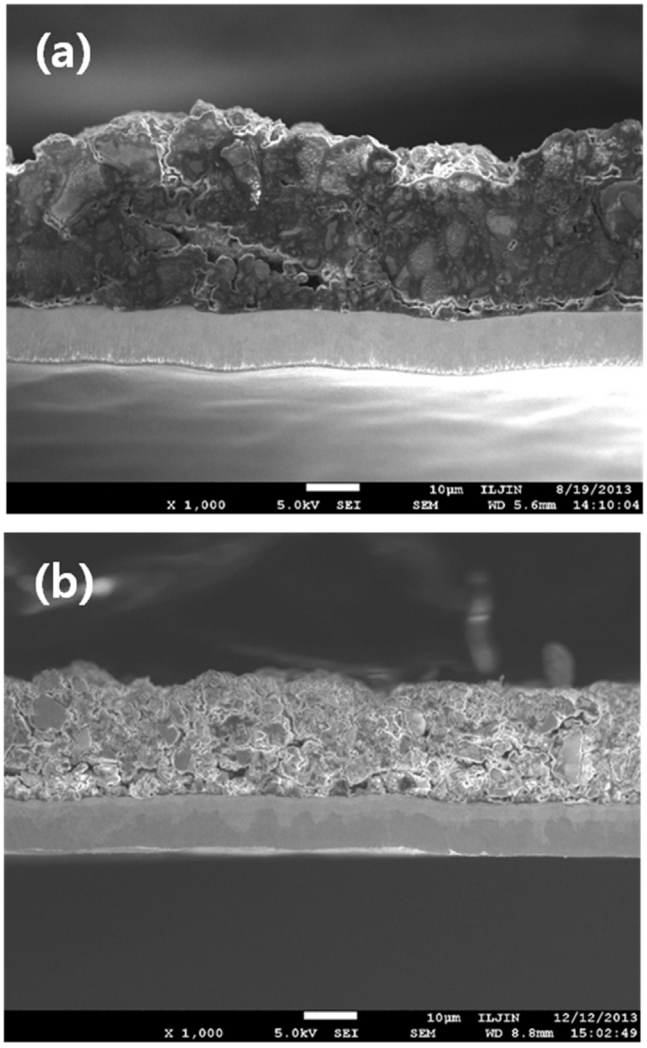

Fig. 7. Cross-sectional SEM images of (a) pristine silicon alloy and (b) rGO(10)-SA electrodes after 100 cycles.

contrast, electrode expansion of the silicon alloy electrode encapsulated by rGO was remarkably reduced, as shown in Fig. 7(b). Furthermore, the electrical contacts between the active materials and copper foil were well maintained in the electrode. These results indicated that rGO coated on the silicon alloy particle buffered against silicon volume changes, and that the good cycling stability of the rGO(10)-SA electrode was closely related to its robust structure during cycling.

The rate capability of the pristine silicon alloy and rGO(x)-SA electrodes was evaluated. The cells were charged to 0.005 V at a constant current rate of 0.2C, followed by a constant voltage charge, and they were then discharged at different current rates ranging from 0.2 to 5.0C. Discharge capacities of the different silicon alloy electrodes for C rates increasing from 0.2 to 5.0C every five cycles are shown in Fig. 8. The effect of rGO coating on the rate performance of the silicon alloy electrodes was noticeable as the current rate was increased to a high rate of 5.0C. Among the various electrodes, the rGO(10)-SA electrode exhibited the best rate capability. At the 5.0C rate, it delivered a discharge capacity of 900.9 mAh g^{-1}, corresponding to 78.7% of the initial discharge capacity at the 0.2C rate. In contrast, the pristine silicon alloy electrode showed a lower discharge capacity of 705.6 mAh g^{-1} at the 5.0C rate. In the silicon alloy electrodes encapsulated by rGO, the coating layer likely prevented the silicon alloy from being

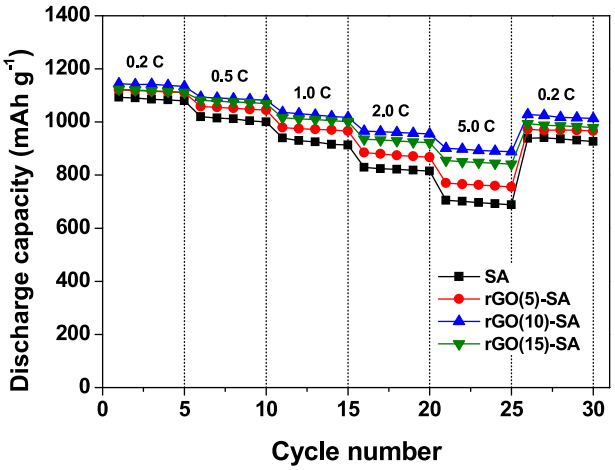

Fig. 8. Discharge capacities of pristine silicon alloy and rGO(x)-SA electrodes as a function of C rate. The C rate was increased from 0.2 to 5.0C after every 5 cycles.

pulverized. Moreover, the highly conductive rGO layer provided a continuous electronic pathway between the silicon alloy particles, which resulted in the observed high rate capability.

4. Conclusions

We demonstrated that the dual strategy of utilizing a silicon alloy with an inert matrix and encapsulating this alloy with rGO enhanced the cycling stability and rate capability of silicon materials for lithium-ion battery applications. We attributed the enhanced cycling performance of the rGO(x)-SA electrode to its unique structure of an alloy encapsulated by a flexible rGO sheet, which allowed the drawbacks of silicon anode materials, namely the large volume changes during cycling, irreversible reactions between silicon and the electrolyte solution, and poor electronic conductivity of the electrode, to be overcome. This strategy is expected to be potentially useful for other electrochemically active materials that suffer from significant volume changes during electrochemical cycling.

Acknowledgements

This work was supported by the Green Industry Leading Secondary Battery Technology Development Program of KEIT (10046341, Development of a high capacity, low cost silicon based anode material for lithium secondary batteries) and by a grant from the Basic Science Research Program through the National Research Foundation of Korea (NRF) funded by the Ministry of Science, ICT, and Future Planning (2014R1A2A2A01002154).

References

[1] M. Armand, J.M. Tarascon, Building better batteries, Nature 451 (2008) 652–657.
[2] N.S. Choi, Z. Chen, S.A. Freunberger, X. Ji, Y.K. Sun, K. Amine, G. Yushin, L.F. Nazar, J. Cho, P.G. Bruce, Challenges facing lithium batteries and electrical double-layer capacitors, Angewandte Chemie—International Edition 51 (2012) 9994–10024.
[3] G. Jeong, Y.-U. Kim, H. Kim, Y.-J. Kim, H.-J. Sohn, Prospective materials and applications for Li secondary batteries, Energy & Environmental Science 4 (2011) 1986–2002.
[4] B. Liang, Y. Liu, Y. Xu, Silicon-based materials as high capacity anodes for next generation lithium ion batteries, Journal of Power Sources 267 (2014) 469–490.
[5] B. Wang, X. Li, B. Luo, L. Hao, M. Zhou, X. Zhang, Z. Fan, L. Zhi, Approaching the downsizing limit of silicon for surface-controlled lithium storage, Advanced Materials 27 (2015) 1526–1532.
[6] B. Key, R. Bhattacharyya, M. Morcrette, V. Seznec, J.-M. Tarascon, C.P. Grey, Real-time NMR investigations of structural changes in silicon electrodes for

lithium-ion batteries, Journal of the American Chemical Society 131 (2009) 9239–9249.
[7] M.T. McDowell, S.W. Lee, W.D. Nix, Y. Cui, Understanding the lithiation of silicon and other alloying anodes for lithium-ion batteries, Advanced Materials 25 (2013) 4966–4985.
[8] J.R. Szczech, S. Jin, Nanostructured silicon for high capacity lithium battery anodes, Energy & Environmental Science 4 (2011) 56–72.
[9] X. Su, Q. Wu, J. Li, X. Xiao, A. Lott, W. Lu, B.W. Sheldon, J. Wu, Silicon-based nanomaterials for lithium-ion batteries: A review, Advanced Energy Materials 4 (2014) 1–23.
[10] M.R. Zamfir, H.T. Nguyen, E. Moyen, Y.H. Lee, D. Pribat, Silicon nanowires for Li-based battery anodes: A review, Journal of Materials Chemistry A 1 (2013) 9566–9586.
[11] H. Wu, Y. Cui, Designing nanostructured Si anodes for high energy lithium ion batteries, Nano Today 7 (2012) 414–429.
[12] M. Ashuri, Q. He, L.L. Shaw, Silicon as a potential anode material for Li-ion batteries: where size, geometry and structure matter, Nanoscale 8 (2016) 74–103.
[13] A.S. Arico, P. Bruce, B. Scrosati, J.-M. Tarascon, W. van Schalkwijk, Nanostructured materials for advanced energy conversion and storage devices, Nature Materials 4 (2005) 366–377.
[14] C. Wang, H. Wu, Z. Chen, M.T. McDowell, Y. Cui, Z. Bao, Self-healing chemistry enables the stable operation of silicon microparticle anodes for high-energy lithium-ion batteries, Nature Chemistry 5 (2013) 1042–1048.
[15] I. Kovalenko, B. Zdyrko, A. Magasinski, B. Hertzberg, Z. Milicev, R. Burtovyy, I. Luzinov, G. Yushin, A major constituent of brown algae for use in high-capacity Li-ion batteries, Science 334 (2011) 75–79.
[16] M.-H. Ryou, J. Kim, I. Lee, S. Kim, Y.K. Jeong, S. Hong, J.H. Ryu, T.-S. Kim, J.-K. Park, H. Lee, J.W. Choi, Mussel-inspired adhesive binders for high-performance silicon nanoparticle anodes in lithium-ion batteries, Advanced Materials 25 (2013) 1571–1576.
[17] H.S. Yang, S.-H. Kim, A.G. Kannan, S.K. Kim, C. Park, D.-W. Kim, Performance enhancement of silicon alloy-based anodes using thermally treated poly (amide imide) as a polymer binder for high performance lithium-ion batteries, Langmuir 32 (2016) 3300–3307.
[18] S.-B. Son, S.C. Kim, C.S. Kang, T.A. Yersak, Y.-C. Kim, C.-G. Lee, S.-H. Moon, J.S. Cho, J.-T. Moon, K.H. Oh, S.-H. Lee, A highly reversible nano-Si anode enabled by mechanical confinement in an electrochemically activated $Li_xTi_4Ni_4Si_7$ matrix, Advanced Energy Materials 2 (2012) 1226–1231.
[19] B.-C. Yu, H.-Y. Kim, C.H. Park, S.K. Kim, J.W. Sung, H.-J. Sohn, Si nano-crystallites embedded in Cu-Al-Fe matrix as an anode for Li secondary batteries, Electrochimica Acta 130 (2014) 583–586.
[20] V. Chabot, K. Feng, H.W. Park, F.M. Hassan, A.R. Elsayed, A. Yu, X. Xiao, Z. Chen, Graphene wrapped silicon nanocomposites for enhanced electrochemical performance in lithium ion batteries, Electrochimica Acta 130 (2014) 127–134.
[21] C. Xu, B. Xu, Y. Gu, Z. Xiong, J. Sun, X.S. Zhao, Graphene-based electrodes for electrochemical energy storage, Energy & Environmental Science 6 (2013) 1388–1414.
[22] N. Lin, J. Zhou, Y. Zhu, Y. Qian, Embedding silicon nanoparticles in graphene based 3D framework by cross-linking reaction for high performance lithium ion batteries, Journal of Materials Chemistry A 2 (2014) 19604–19608.
[23] J. Chang, X. Huang, G. Zhou, S. Cui, P.B. Hallac, J. Jiang, P.T. Hurley, J. Chen, Multilayered Si nanoparticle/reduced graphene oxide hybrid as a high-performance lithium-ion battery anode, Advanced Materials 26 (2014) 758–764.
[24] X. Gao, J. Li, Y. Xie, D. Guan, C. Yuan, A multilayered silicon-reduced graphene oxide electrode for high performance lithium-ion batteries, ACS Applied Materials & Interfaces 7 (2015) 7855–7862.
[25] H. Yue, S. Wang, Z. Yang, Q. Li, S. Lin, D. He, Ultra-thick porous films of graphene-encapsulated silicon nanoparticles as flexible anodes for lithium ion batteries, Electrochimica Acta 174 (2015) 688–695.
[26] X. Zhou, Y.-X. Yin, L.-J. Wan, Y.-G. Guo, Self-assembled nanocomposite of silicon nanoparticles encapsulated in graphene through electrostatic attraction for lithium-ion batteries, Advanced Energy Materials 2 (2012) 1086–1090.
[27] R. Hu, W. Sun, Y. Chen, M. Zeng, M. Zhu, Silicon/graphene based nanocomposite anode: large-scale production and stable high capacity for lithium ion batteries, Journal of Materials Chemistry A 2 (2014) 9118–9125.
[28] N. Li, S. Jin, Q. Liao, H. Cui, C.X. Wang, Encapsulated within graphene shell silicon nanoparticles anchored on vertically aligned graphene trees as lithium ion battery anodes, Nano Energy 5 (2014) 105–115.
[29] B. Wang, X. Li, X. Zhang, B. Luo, M. Jin, M. Liang, S.A. Dayeh, S.T. Picraux, L. Zhi, Adaptable silicon carbon nanocables sandwiched between reduced graphene oxide sheets as lithium ion battery anodes, ACS Nano 7 (2013) 1437–1445.
[30] M. Zhou, X. Li, B. Wang, Y. Zhang, J. Ning, Z. Xiao, X. Zhang, Y. Chang, L. Zhi, High-performance silicon battery anodes enabled by engineering graphene assemblies, Nano Letters 15 (2015) 6222–6228.
[31] A.G. Kannan, S.-H. Kim, H.S. Yang, D.-W. Kim, Silicon nanoparticles grown on reduced graphene oxide surface as high performance anode materials for lithium-ion batteries, RSC Advances 6 (2016) 25159–25166.
[32] N.I. Kovtyukhova, P.J. Ollivier, B.R. Martin, T.E. Mallouk, S.A. Chizhik, E.V. Buzaneva, A.D. Gorchinskiy, Layer-by-layer assembly of ultrathin composite films from micron-sized graphite oxide sheets and polycations, Chemistry of Materials 11 (1999) 771–778.
[33] W.S. Hummers, R.E. Offeman, Preparation of graphitic oxide, Journal of the American Chemical Society 80 (1958) 1339–1339.
[34] M. Yan, F. Wang, C. Han, X. Ma, X. Xu, Q. An, L. Xu, C. Niu, Y. Zhao, X. Tian, P. Hu, H. Wu, L. Mai, Nanowire templated semihollow bicontinuous graphene scrolls: Designed construction, mechanism, and enhanced energy storage performance, Journal of the American Chemical Society 135 (2013) 18176–18182.
[35] J.-H. Kim, A.G. Kannan, H.-S. Woo, D.-G. Jin, W. Kim, K. Ryu, D.-W. Kim, A bi-functional metal-free catalyst composed of dual-doped graphene and mesoporous carbon for rechargeable lithium-oxygen batteries, Journal of Materials Chemistry A 3 (2015) 18456–18465.
[36] C.H. Lim, A.G. Kannan, H.-W. Lee, D.K. Kim, A high power density electrode with ultralow carbon via direct growth of particles on graphene sheets, Journal of Materials Chemistry A 1 (2013) 6183–6190.
[37] M.N. Obrovac, V.L. Chevrier, Alloy negative electrodes for Li-Ion batteries, Chemical Reviews 114 (2014) 11444–11502.
[38] S.-L. Chou, J.-Z. Wang, M. Choucair, H.-K. Liu, J.A. Stride, S.-X. Dou, Enhanced reversible lithium storage in a nanosize silicon/graphene composite, Electrochemistry Communications 12 (2010) 303–306.
[39] X. Chen, X. Li, F. Ding, W. Xu, J. Xiao, Y. Cao, P. Meduri, J. Liu, G.L. Graff, J.-G. Zhang, Conductive rigid skeleton supported silicon as high-performance Li-ion battery anodes, Nano Letters 12 (2012) 4124–4130.
[40] N. Liu, K. Huo, M.T. McDowell, J. Zhao, Y. Cui, Rice husks as a sustainable source of nanostructured silicon for high performance Li-ion battery anodes, Scientific Reports 3 (2013) 1919–1925.